



# Induced chirality in micron wave through electromagnetic coupling between chiral molecules and graphene nanostructures



Yongkai Wang, Tong Fu, Tiankun Wang, Yongfang Li, Zhongyue Zhang\*

School of Physics and Information Technology, Shaanxi Normal University, Xi'an 710062, China

## ARTICLE INFO

### Article history:

Received 20 January 2017

Received in revised form

14 April 2017

Accepted 10 May 2017

Available online 13 May 2017

## ABSTRACT

The intricate mechanisms of plasmon-induced circular dichroism (CD) in a visible region are considered based on chemical and physical influences, in which a simple model and formulations are required. Here, we demonstrate theoretically that plasmon-induced CD is approximately contributed by the cross-interaction between equivalent electric and magnetic dipole moments for chiral molecules and plasmon nanostructures. To prove electromagnetic couplings, we introduce graphene into plasmon nanostructures and design asymmetrically inscribed graphene dual-rings arrays (IGDAs) with high-order hybrid modes. Results show that ultrahigh-order plasmon-induced CD signals are achieved in micron wave, which is easily detected by mature microwave technology. The maximum enhancement factor of induced CD could reach up to four orders of magnitude. In addition, an induced CD signal could be tuned only by varying the Fermi energy of IGDAs rather than by varying geometric dimensions. For different molecules, the electromagnetic couplings still hold. The results could be used to dynamically design chiral sensors in biology and chemistry.

© 2017 Elsevier Ltd. All rights reserved.

## 1. Introduction

Chiral structures cannot be made to coincide with their mirror images. In 1969, Sherman demonstrated the optical property of chiral chlorophyll-a, which presents different optical responses to right circularly polarized (RCP, +) and left circularly polarized (LCP, -) light [1], i.e., circular dichroism (CD) [2–4]. CD spectroscopic techniques probe the molecular conformation, but suffer from poor sensitivity [5,6]. Meanwhile, surface plasmon-based near-field enhancement delivered through specifically designed substrates is highly successful for ultrasensitive optical biosensor applications [7,8], such as surface-enhanced Raman spectroscopy (SERS) [9]. However, SERS lack conformational information about the molecules, such as information about molecular chirality.

Recently, experimental [10–13] and theoretical [14–16] research has reported on the interaction between chiral molecules and metal nanostructures for inducing chiral signals of molecules from UV spectral to visible regions. The CD enhancement factors of chiral molecules and metal nanostructures reach up to 1000 [17]. The reason for this finding is attributed to physical

reasons, such as the plasmon-generated superchiral near fields [18–20] or induced optical activity due to near fields, both at isolated plasmonic nanostructures and at hotspots between the gap of nanostructures [21,22]. In the experiment, the reason for this finding is attributed to chemical reasons, such as the charge transfer to a plasmonic nanostructure through bonds formed by chemisorbed analyses [23]. Interband-absorption-enhanced unusual CD band can originate from conformational changes of the chemisorbed molecules [24].

The abovementioned phenomenon opens novel opportunities in ultrasensitive probing of chiral molecules and for novel optical nanomaterials based on chiral elements. However, the mechanism of induced CD signals is complex and ambiguous. Therefore, a simple model and formulations are required to understand the reasons for induced CD. In addition, all the induced CD signals reported above are present around visible regions. If the CD signals were induced around micron wave regions, chiral molecules could be detected more easily than at around visible regions. These results stem from mature microwave technologies that have been applied in electronics systems. The graphene has successfully applied in micron wave [25]. We can use graphene to replace metallic material in nanophotonics. Asymmetric placed rings can show many high-order hybrid modes when they interact with each other, which can be selective detected in a long region.

\* Corresponding author.

E-mail address: [zyzhang@snnu.edu.cn](mailto:zyzhang@snnu.edu.cn) (Z. Zhang).

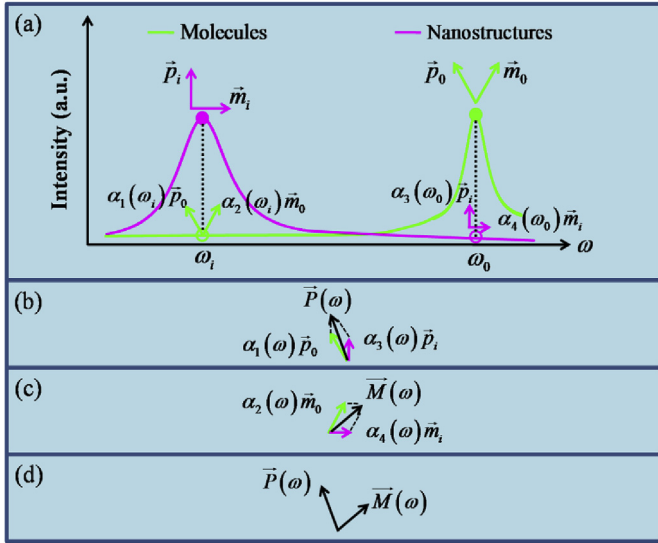


**Fig. 1.** Schematic of electromagnetic coupling between chiral molecules (green line) and plasmon nanostructures (magenta line): (a) the normalized intensities of equivalent electric and magnetic dipole moments, the vector resultant of electric (b) and magnetic (c) dipole moments, (d) the total electric and magnetic dipole moments. (A colour version of this figure can be viewed online.)

In this study, we demonstrate theoretically that plasmon-induced CD approximately contributes to the cross-interaction between equivalent electric and magnetic dipole moments for chiral molecules and plasmon nanostructures. To prove the electromagnetic couplings, we introduce graphene into plasmon nanostructures and design asymmetrical inscribed graphene dual-ring arrays (IGDAs) with high-order hybrid modes. Results show that ultrahigh-order plasmon-induced CD signals are achieved in the micron wave, which is easily detected by mature microwave technology. The maximum enhancement factor of induced CD could reach up to four orders of magnitude. In addition, the induced CD signal could be tuned only by varying the Fermi energy of IGDAs

$$\begin{aligned} \text{CD}_{\text{molecule+plasmon}}(\omega) \propto & \text{Im} \left[ \left( e^{-(\omega-\omega_0)^2/\sigma_1} \vec{p}_0 + e^{-(\omega-\omega_i)^2/\sigma_3} \vec{p}_i \right) \cdot \left( e^{-(\omega-\omega_0)^2/\sigma_2} \vec{m}_0 + e^{-(\omega-\omega_i)^2/\sigma_4} \vec{m}_i \right) \right] \\ & \propto \text{Im} \left[ e^{-(\omega-\omega_0)^2(1/\sigma_1+1/\sigma_2)} \vec{p}_0 \cdot \vec{m}_0 + e^{-(\omega-\omega_0)^2/\sigma_1-(\omega-\omega_i)^2/\sigma_4} \vec{p}_0 \cdot \vec{m}_i + e^{-(\omega-\omega_0)^2/\sigma_2-(\omega-\omega_i)^2/\sigma_3} \vec{m}_0 \cdot \vec{p}_i \right], \end{aligned} \quad (3)$$

rather than by varying geometric dimensions. For different molecules, the electromagnetic couplings still hold.

## 2. Theory

Fig. 1(a) shows the normalized intensities of equivalent electric and magnetic dipole moments for chiral molecules (green line) and plasmon nanostructures (magenta line) and are described as two functions of  $\omega$ , which is the angular frequency of incident light. The resonant absorptions of chiral molecules and plasmon nanostructures are  $\omega_0$  and  $\omega_i$ , respectively. For chiral molecules at  $\omega_0$ , the resonant electric and magnetic dipole moments of chiral molecules are labeled as  $\vec{p}_0$  and  $\vec{m}_0$ , respectively. Given the chirality of molecules,  $\vec{p}_0 \cdot \vec{m}_0 \neq 0$ , which do not form a right angle between  $\vec{p}_0$  and  $\vec{m}_0$ . For plasmon nanostructures at  $\omega_i$ , the resonant electric and magnetic dipole moments of plasmon nanostructures are labeled

as  $\vec{p}_i$  and  $\vec{m}_i$ , respectively. As a result of the achirality of plasmon nanostructures,  $\vec{p}_i \cdot \vec{m}_i = 0$ , which forms a right angle between  $\vec{p}_i$  and  $\vec{m}_i$ .

The normalized intensities of electric and magnetic dipole moments decay from resonant angular frequencies to non-resonant angular frequencies. The decayed coefficient is defined as  $\alpha(\omega) \propto 1/(\omega - \omega_0)^2$  [16]. The coefficient will reach infinity at  $\omega = \omega_0$ , which is not a reality in physical systems. In this study, decay coefficients with the form  $e^{-(\omega-\omega_0)^2/\sigma}$  is proposed and proved in the Results and Discussion section. Decayed coefficients of electric dipole moments of chiral molecules are defined as  $\alpha_1(\omega) = e^{-(\omega-\omega_0)^2/\sigma_1}$ ,  $\alpha_2(\omega) = e^{-(\omega-\omega_0)^2/\sigma_2}$  for magnetic dipole moments of chiral molecules,  $\alpha_3(\omega) = e^{-(\omega-\omega_0)^2/\sigma_3}$  for electric dipole moments of plasmon nanostructures, and  $\alpha_4(\omega) = e^{-(\omega-\omega_0)^2/\sigma_4}$  for magnetic dipole moments of plasmon nanostructures. At  $\omega_i$ ,  $\vec{p}_0$  and  $\vec{m}_0$  decay into  $\alpha_1(\omega_i) \vec{p}_0$  and  $\alpha_2(\omega_i) \vec{m}_0$ , respectively. At  $\omega_0$ ,  $\vec{p}_i$  and  $\vec{m}_i$  decay into  $\alpha_3(\omega_0) \vec{p}_i$  and  $\alpha_4(\omega_0) \vec{m}_i$ , respectively.

The quantum theory of the CD effect of chiral molecules is described as a  $\omega$  function [26,27].

$$\text{CD}_{\text{molecules}}(\omega) \propto \text{Im} [\alpha_1(\omega) \vec{p}_0 \cdot \alpha_2(\omega) \vec{m}_0]. \quad (1)$$

When plasmon nanostructures are introduced into chiral molecules, the total electric dipole moments  $\vec{P}(\omega)$  can be composited by  $\alpha_1(\omega) \vec{p}_0$  and  $\alpha_3(\omega) \vec{p}_i$ , as shown in Fig. 1(b). The total magnetic dipole moments  $\vec{M}(\omega)$  can be composited by  $\alpha_2(\omega) \vec{m}_0$  and  $\alpha_4(\omega) \vec{m}_i$ , as shown in Fig. 1(c). Therefore, as shown in Fig. 1(d), the CD effect of chiral molecules and plasmon nanostructures is described as a general equation

$$\begin{aligned} \text{CD}_{\text{molecule+plasmon}}(\omega) \propto & \text{Im} [\vec{P}(\omega) \cdot \vec{M}(\omega)] \propto \text{Im} [( \alpha_1(\omega) \vec{p}_0 \\ & + \alpha_3(\omega) \vec{p}_i ) \cdot ( \alpha_2(\omega) \vec{m}_0 + \alpha_4(\omega) \vec{m}_i ) ] \end{aligned} \quad (2)$$

Taking  $\alpha_1$  and  $\alpha_2$  into Eq. (2), the CD effect of chiral molecules and plasmon nanostructures is described as

where  $e^{-(\omega-\omega_i)^2/\sigma_3-(\omega-\omega_i)^2/\sigma_4} \vec{p}_i \cdot \vec{m}_i = 0$  because of  $\vec{p}_i \cdot \vec{m}_i = 0$  for achiral plasmon nanostructures. When  $\omega = \omega_0$ , Eq. (3) is reduced into

$$\begin{aligned} \text{CD}_{\text{molecule+plasmon}}(\omega_0) \propto & \text{Im} \left[ \vec{p}_0 \cdot \vec{m}_0 + e^{-(\omega_0-\omega_i)^2/\sigma_4} \vec{p}_0 \cdot \vec{m}_i \right. \\ & \left. + e^{-(\omega_0-\omega_i)^2/\sigma_3} \vec{m}_0 \cdot \vec{p}_i \right]. \end{aligned} \quad (4)$$

Given CD lines of chiral molecules in the UV region and plasmon bands of nanostructures in the visible or infrared regions, then  $(\omega_i - \omega_0)^2 \gg 0$ . Therefore,  $e^{-(\omega_0-\omega_i)^2/\sigma_4} \vec{p}_0 \cdot \vec{m}_i$  and  $e^{-(\omega_0-\omega_i)^2/\sigma_3} \vec{m}_0 \cdot \vec{p}_i$  could be ignored because they are of a higher order infinitesimal with respect to  $\vec{p}_0 \cdot \vec{m}_0$ . Therefore, Eq. (3) could be approximated as

$$CD_{molecule+plasmon}(\omega_0) \propto \text{Im} [\vec{p}_0 \cdot \vec{m}_0]. \quad (5)$$

Equation (5) means that in the UV region, the CD signals of chiral molecules and plasmon nanostructures approximately equal the CD signals of the chiral molecules alone.

When  $\omega = \omega_i$ , Eq. (3) is reduced as

$$CD_{molecule+plasmon}(\omega_i) \propto \text{Im} \left[ e^{-(\omega_i - \omega_0)^2 (1/\sigma_1 + 1/\sigma_2)} \vec{p}_0 \cdot \vec{m}_0 + e^{-(\omega_i - \omega_0)^2 / \sigma_1} \vec{p}_0 \cdot \vec{m}_i + e^{-(\omega_i - \omega_0)^2 / \sigma_2} \vec{m}_0 \cdot \vec{p}_i \right]. \quad (6)$$

$e^{-(\omega_i - \omega_0)^2 (1/\sigma_1 + 1/\sigma_2)} \vec{p}_0 \cdot \vec{m}_0$  can be ignored because of the higher order infinitesimal with respect to  $e^{-(\omega_i - \omega_0)^2 / \sigma_1} \vec{p}_0 \cdot \vec{m}_i$  and  $e^{-(\omega_i - \omega_0)^2 / \sigma_2} \vec{m}_0 \cdot \vec{p}_i$ . Therefore, Eq. (6) could be approximated as

$$CD_{molecule+plasmon}(\omega_i) \propto \text{Im} [\alpha_1(\omega_i) \vec{p}_0 \cdot \vec{m}_i + \alpha_2(\omega_i) \vec{m}_0 \cdot \vec{p}_i]. \quad (7)$$

Equation (7) means that induced CD signals could be approximated as a cross-interaction between equivalent electric and magnetic dipole moments for chiral molecules and plasmon nanostructures. When  $|\omega_0 - \omega_i| \gg 0$ , the induced CD signals in the plasmon region originate from long-range electromagnetic coupling between the chiral molecules and the plasmon nanostructures, and are weaker than the CD signals of the chiral molecules alone. The model can also help us understand electromagnetic coupling between chiral molecules and chiral plasmonic nanostructures, such as stacked-patch plasmonic metamaterial [28].

### 3. Structure and computational method

To prove the electromagnetic coupling above and induce CD signals in microwave technology, graphene is introduced into the system of chiral molecules and plasmon nanostructures. The particular geometries of chiral molecules are hardly controlled in practice. Therefore, the molecules are regarded as a homogeneous and isotropic chiral medium layer in our model that can be realized using chiral solution. Fig. 2(a) shows the proposed monolayer IGDA and chiral molecules. IGDA (gray) are immersed in the chiral molecular solution (blue), whose thickness is fixed at  $t = 300$  nm. IGDA are composed of inscribed graphene dual-rings. The diameters of the inner and outer rings are fixed at  $d = 90$  nm and  $D = 190$  nm, respectively. The widths of the inner and outer rings are both fixed at  $w = 10$  nm. Fig. 2(b) shows the magnified

surface of IGDA. Hexagon arrays (gray) and double helix (blue) denote the monolayer graphene and chiral molecules, respectively. The periods in the  $x$  and  $y$  directions are fixed at  $P_x = 300$  nm and  $P_y = 300$  nm, respectively. The infinite array is simulated by using a unit cell with periodic boundary conditions along the  $x$  and  $y$  directions. LCP (red) and RCP lights (green) along the  $z$ -direction excite on IGDA and form enhanced fields on the surface of IGDA. Transmittance is defined as  $T = P_{\text{out}}/P_{\text{in}}$ , which is the ratio of output power to incident power. The transmittance spectra of RCP light and LCP light are represented by  $T_{++}$  and  $T_{--}$ , respectively. Here, we use  $CD = T_{++} - T_{--}$  to define the chiral response of IGDA and chiral molecules.

The finite element method (FEM) software COMSOL Multiphysics is used to perform the simulation. The general constitutive relations for chiral material can be written as

$$\vec{D} = \epsilon_0 \epsilon \vec{E} - \frac{ik}{c} \vec{H}, \quad (8)$$

$$\vec{B} = \mu_0 \mu \vec{H} + \frac{ik}{c} \vec{E}. \quad (9)$$

Here,  $\vec{D}$ ,  $\vec{H}$ ,  $\vec{E}$ , and  $\vec{B}$  are complex electric displacement, magnetic field strength, electric and magnetic fields, respectively.  $c$  is the speed of light in vacuum. The dimensionless parameters  $\epsilon$  and  $\mu$  involved here are permittivity and permeability. Pasteur parameter  $\kappa$  denotes the chirality index of chiral material, because  $\kappa$  controls the coupling strength between electric and magnetic. The chiral molecules are simulated by the following modeled as [29].

$$\epsilon = \epsilon_b - \gamma \left( \frac{1}{\hbar\omega - \hbar\omega_0 + i\Gamma} - \frac{1}{\hbar\omega + \hbar\omega_0 + i\Gamma} \right), \quad (10)$$

$$\kappa = \beta \left( \frac{1}{\hbar\omega - \hbar\omega_0 + i\Gamma} - \frac{1}{\hbar\omega + \hbar\omega_0 + i\Gamma} \right), \quad (11)$$

Here,  $\epsilon_b$  denotes the refractive index of background, the chiral molecules are generally dissolved in water for measurement, thus, water is taken as background and  $\epsilon_b = 1.332$ . The amplitudes of absorption and chirality of real molecules are defined as coefficients  $\gamma \approx 1.4 \times 10^{-5}$  and  $\beta \approx 3 \times 10^{-9}$ , respectively. For reducing the computational time, we scale up orders of two coefficients as  $\gamma \approx 7 \times 10^{-2}$  and  $\beta \approx 6 \times 10^{-4}$ . When the ratio between  $\kappa$  and  $\epsilon$  is small, above scaled up orders are not affected the enhancement factors, which is usually the case for realistic chiral analytes. The absorption broadening is determined by  $\Gamma = 0.1$  eV. When taking the right-hand circular polarized (RCP, +) light and

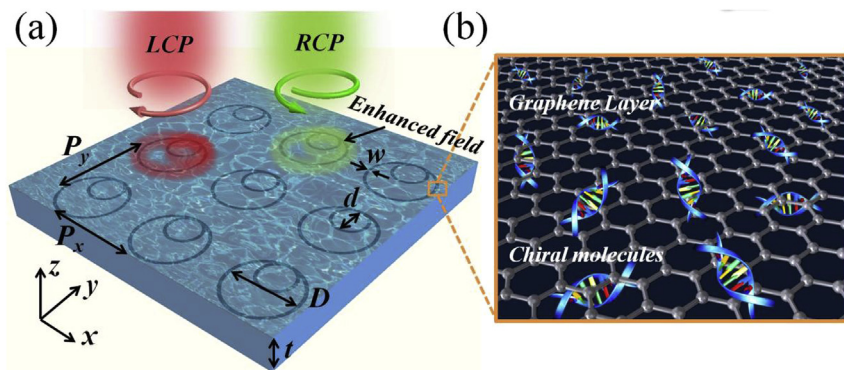


**Fig. 2.** (a) Schematic of IGDA immersed in chiral molecular solution and parameters definition, and (b) the zoom cell presenting graphene layer and chiral molecules. (A colour version of this figure can be viewed online.)

left-hand circular polarized (LCP,  $-$ ) light into consideration, the effective refractive indices of chiral media are [30].

$$n_{\pm} = \sqrt{\varepsilon\mu \pm \kappa}. \quad (12)$$

The conductivity of graphene is a function of the frequency of incident light and computed within the local random phase approximation [31–33].

$$\sigma(\omega) = \frac{2ie^2k_B T}{\pi\hbar^2(\omega + i\tau^{-1})} \ln \left[ 2 \cosh \left( \frac{E_f}{2k_B T} \right) \right] + \frac{e^2}{4\hbar} \left\{ \frac{1}{2} + \frac{1}{\pi} \arctan \left( \frac{\hbar\omega - 2E_f}{2k_B T} \right) - \frac{i}{2\pi} \ln \left[ \frac{(\hbar\omega + 2E_f)^2}{(\hbar\omega - 2E_f)^2 + (2k_B T)^2} \right] \right\}, \quad (13)$$

where  $e$ ,  $\hbar$ ,  $k_B$ , and  $E_f$  correspond to the electron charge, reduced Planck constant, Boltzmann constant, and Fermi energy (gate voltage), respectively. The carrier relaxation  $\tau = \frac{\rho E_f}{e v_F}$ ,  $v_F$  is Fermi velocity, and  $\rho$  is the measured DC mobility,  $\rho = 10000 \text{ cm}^2/\text{V}$  [34]. In our study, Eq. (13) is simulated at  $T = 300 \text{ K}$ , and  $k_B \times T$  refers to temperature energy. The first term in Eq. (13) corresponds to intra-band electron–photon scattering processes. The second term represents the inter-band transition contribution. For the second term, the function of arctangent is a step function. The expression shows that the inter-band contribution becomes dominant at a frequency of  $\omega > E_f$  because of the absence of a gap between conduction and valence bands. When  $\omega < E_f$ , the opposite case is evident; likewise,

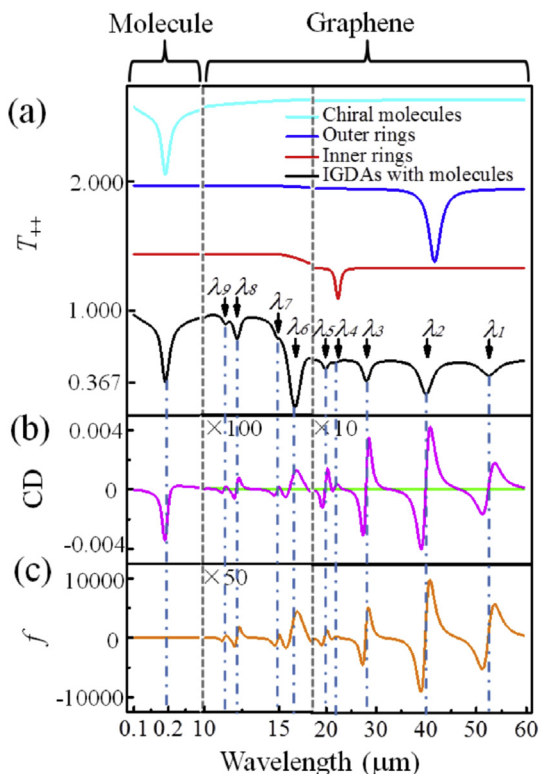
the intra-band contribution is dominant [35,36].

#### 4. Results and discussion

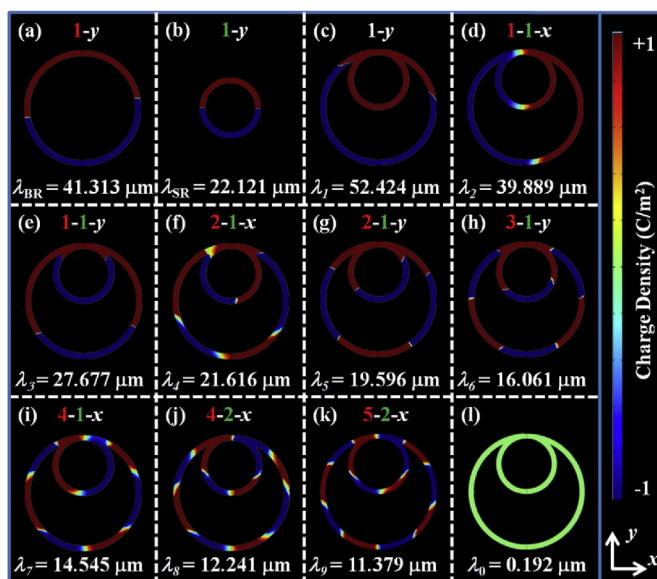
Fig. 3(a) shows the  $T_{++}$  of chiral molecules, outer rings, inner rings, and IGDA with chiral molecules. Here, chiral molecular absorption wavelength  $\lambda_0 = 0.192 \mu\text{m}$ , and graphene Fermi energy  $E_f = 0.50 \text{ eV}$ . The wavelength region is from 0.1 to 60  $\mu\text{m}$ . To observe all characteristics of  $T_{++}$ , we divide the entire spectrum into three segments, namely, 0.1–0.3  $\mu\text{m}$ , 10–17  $\mu\text{m}$ , and 17–60  $\mu\text{m}$ . Every segment transmittance has different scales. The regions of 0.1–0.3  $\mu\text{m}$  and 10–60  $\mu\text{m}$  present the characteristics of chiral molecule and graphene, respectively. The  $T_{++}$  of chiral molecules, inner rings, and outer rings presents three resonant dips in  $\lambda_0 = 0.192 \mu\text{m}$ ,  $\lambda_{IR} = 22.084 \mu\text{m}$ , and  $\lambda_{OR} = 41.131 \mu\text{m}$ , respectively. We composite inner and outer rings into asymmetrical IGDA with chiral molecules, whose  $T_{++}$  (black line) is shown in Fig. 3(a). New resonant dips denoted by  $\lambda_i$  ( $i$  is from “1” to “9”) are observed between 10 and 60  $\mu\text{m}$  as a result of the hybridization between inner and outer rings that form high-order hybrid modes. The resonant dip of chiral molecules is observed at  $\lambda_0 = 0.192 \mu\text{m}$ .  $T_{++}$  above similarly corresponds to  $T_{--}$ , which is not shown in here.

Fig. 3(b) shows the CD spectra of chiral molecules alone (green line) and IGDA with chiral molecules (pink line), respectively. To present all CD spectra clearly, induced CD signals are artificially amplified by 100 and 10 times at 10–17 and 17–60  $\mu\text{m}$ , respectively. The CD spectrum of chiral molecules alone and IGDA with chiral molecules almost overlap at the dip at  $\lambda_0 = 0.192 \mu\text{m}$ . However, the CD spectrum of IGDA with chiral molecules represents new signals around the micron wave, where resonant absorption wavelengths  $\lambda_i$  of IGDA emerge. New CD signals at  $\lambda_i$  are defined as induced CD. As interpreted by Eqs. (5) and (7), the induced CD at around micron wave is weaker than that of chiral molecules in the UV region. A comparison between the results from Eq. (7) and those in Fig. 3(b) (magenta line) is shown in the Supplementary data file (Fig. S1).

To quantify such enhancement phenomena, we define the CD enhancement factor  $f$  as the ratio between the values of the CD signals of IGDA with chiral molecules and chiral molecules alone,



**Fig. 3.** (a)  $T_{++}$  of chiral molecules, outer rings, inner rings, and IGDA with chiral molecules; (b) CD spectra of chiral molecules alone (green line) and with IGDA (magenta line); (c) the CD enhancement factor  $f$  as the ratio between the values of magenta line and with green line. (A colour version of this figure can be viewed online.)



**Fig. 4.** The charge distributions (color distributions) at resonant wavelengths for (a) outer ring alone, (b) inner rings alone, and (c)–(l) IGDA with chiral molecules. (A colour version of this figure can be viewed online.)

as shown in Fig. 3(c). Correlation is positive between  $f$  and CD signals. The maximum  $f$  at two sides of  $\lambda_i$  increases to the order of  $10^4$  at  $\lambda_2$ .  $f$  is magnified by 50 times at 10–17  $\mu\text{m}$  for easy observation. Given that CD lines almost overlap at 0.1–0.3  $\mu\text{m}$  in Fig. 3(b), the  $f$  approximate one at this region is shown in Fig. 3(c).

In Fig. 3,  $f$  is clearly tied with the effect of resonant absorption of IGDA. For different  $\lambda_i$ , normalized charge distributions on the surface of IGDA are calculated. Fig. 4(a) and (b) show the single outer ring and single inner ring, respectively, while Figs. 4(c)–(l) show the IGDA with chiral molecules. Red indicates positive charge, and blue indicates negative charge. We define the dipolar mode as  $MN = 1$ . The quadrupolar, octupolar, hexadecapolar, and triakontadipolar modes correspond to  $MN = 2$ ,  $MN = 3$ ,  $MN = 4$ , and  $MN = 5$ , respectively. Fig. 4(a) and (b) show that, because the charges on the outer ring alone and the inner ring alone could be equivalent to two dipoles along the  $y$ -direction (labeled as “ $y$ ”), the dipoles could be labeled with “1” (red for the outer ring, green for the inner ring). To break the symmetry of the outer ring, high-order hybrid modes of IGDA are achieved at  $\lambda_i$ . For  $\lambda_1$ , Fig. 4(c) shows a dipole of whole IGDA almost along the  $y$ -direction, which are labeled as “1- $y$ .” For  $\lambda_2$ , Fig. 4(d) shows dipoles of outer and inner rings along the  $x$ -direction, which are labeled as “1-1- $x$ .” For  $\lambda_3$ , Fig. 4(e) shows dipoles of outer and inner rings along  $y$ -direction, which are labeled as “1-1- $y$ .” Analogously, in Fig. 4(f)–(k),  $\lambda_4$ ,  $\lambda_5$ ,  $\lambda_6$ ,  $\lambda_7$ ,  $\lambda_8$ , and  $\lambda_9$  are labeled as “2-1- $x$ ,” “2-1- $y$ ,” “3-1- $y$ ,” “4-1- $x$ ,” “4-2- $x$ ,” and “5-2- $x$ ,” respectively. Detailed descriptions about these high-order hybrid modes [37,38] are shown in Supplementary data file (Fig. S2). Fig. 4(l) shows non-resonant charge distribution, which results in a very small  $f$  at  $\lambda_0$ .

To probe induced CD signals conveniently in different microwave regions, we can only change  $E_f$  by holding on the power on

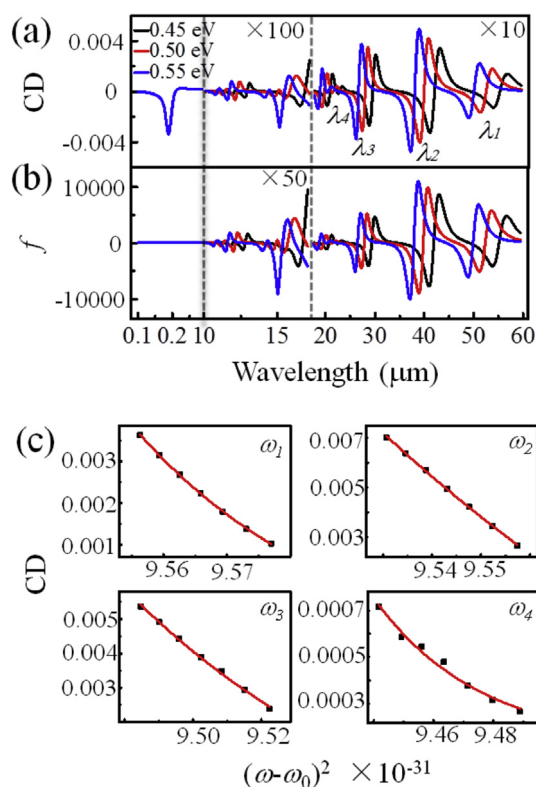


Fig. 5. (a) CD spectra; (b)  $f$  spectra; (c) numerical (black squares) and exponential fitting (red lines)  $\text{CD}_{\text{molecule+plasmon}}(\omega_i)$  ( $i = 1, 2, 3$ , and 4) of IGDA with chiral molecules for different  $E_f$ . (A colour version of this figure can be viewed online.)

IGDA, which is immersed in a chiral molecular solution, as shown in Fig. 5. To reprepare IGDA with different geometric parameters is unnecessary for tuning induced CD signals. Fig. 5(a) and (b) show the CD and CD enhancement factor spectra for IGDA with chiral molecules with different  $E_f$ s from 0.45 to 0.55 eV, respectively. The spectrum in the UV region does not shift with the increase in  $E_f$  because  $\lambda_0$  is decided by chiral molecules. The spectra in the microwave region blue shifts with the increase in  $E_f$ . The behavior of the blue shift can be clarified as the resonance condition of surface plasmons. Resonant frequency  $f_i$  of IGDA could be approximately described as a function of Fermi energy  $\sqrt{E_f}$  because the wave vector of the surface plasmons along the graphene layer is expressed as [39].

$$k_i = \frac{2\pi}{\lambda_i} \propto \frac{\hbar^2 f_i^2}{2e^2 E_f} \quad (14)$$

Taking  $\lambda_i = \frac{c}{f_i}$  into Eq. (14), we obtain the function as

$$\lambda_i \propto \frac{\hbar^2 c^2}{4\pi e^2 E_f} \quad (15)$$

According to Eq. (15),  $\lambda_i$  decreases with an increase in  $E_f$ , as shown in Fig. 5(a) and (b). The magnitudes of spectra in the induced region increase with the decrease in  $\lambda_i$ . This effect is due to the decreased  $\lambda_i$  that lessens  $(\omega_0 - \omega_i)^2$ , which then increases  $\alpha_2$ . According to Eq. (7), the electromagnetic coupling between IGDA and chiral molecules would then increase. In addition, numerical (black squares) and exponential fitting (red lines)  $\text{CD}_{\text{molecule+plasmon}}(\omega_i)$  ( $i = 1, 2, 3$ , and 4) of IGDA with chiral molecules indicate different  $E_f$  that range from 0.40 eV to 0.70 eV, as shown in Fig. 5(c). Results show that  $\text{CD}_{\text{molecule+plasmon}}(\omega_i)$  is an exponential decay function of  $(\omega_0 - \omega_i)^2$ , which indicates reasonable rationality exponential decay approximation in Eq. (7).

To analyze the effects of different chiral molecules on electromagnetic coupling between IGDA and chiral molecules, we sequentially vary  $\lambda_0$  from 0.162  $\mu\text{m}$  to 222  $\mu\text{m}$  with fixed  $E_f = 0.50$  eV. Fig. 6(a) and (b) show the CD spectra and corresponding  $f$  spectra of IGDA with chiral molecules with different  $\lambda_0$ , respectively. In Fig. 6(a), the zoom shows the CD spectra at 49–51  $\mu\text{m}$  to represent the small change. The CD spectra in the UV region red shift shows an increase in  $\lambda_0$ , which is decided by chiral molecules. The CD spectra and corresponding  $f$  spectra in the induced region hardly shift with the increase in  $\lambda_0$  because induced chirality is mainly decided by  $\lambda_i$ . The magnitudes of CD spectra in

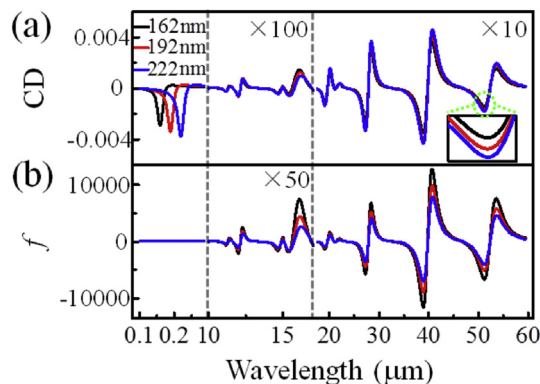


Fig. 6. (a) CD and (b)  $f$  spectra of IGDA with chiral molecules for different  $\lambda_0$ . (A colour version of this figure can be viewed online.)

the induced region increase with an increase in  $\lambda_0$ . The increase in  $\lambda_0$  increases  $\alpha_1$  according to Eq. (7), and thus, electromagnetic coupling between IGDA and chiral molecules increases as well. Similar results occur when graphene is replaced by silver, as shown in Supplementary data file (Figs. S3 and S4).

## 5. Conclusions

We proposed a theoretical model of plasmon-induced CD and demonstrated that the model approximately contributes to the cross interaction between equivalent electric and magnetic dipole moments for chiral molecules and plasmon nanostructures. To prove the proposed theory, we introduced graphene into plasmon nanostructures and designed asymmetrical IGDA with high-order hybrid modes. Results showed that ultrahigh-order plasmon-induced CD signals are achieved in the broadband microwave region, which is easily detected by mature microwave technology. The maximum enhancement factor of induced CD could reach up to four orders of magnitude. In addition, the induced CD signal could be tuned only by varying the Fermi energy of IGDA rather than by varying geometric dimensions. For different molecules, the electromagnetic couplings still hold. The results could elucidate the induced CD mechanism and be used to design dynamically chiral sensors with the power of graphene in biology and chemistry.

## Acknowledgements

This work was supported by National Natural Foundation of China (Grant No. 61575117), Fundamental Research Funds for the Central Universities of Ministry of Education of China (Grant No. GK201601008), and Foundation for Excellent PhD Dissertation of Shaanxi Normal University (NO. X2014YB08).

## Appendix A. Supplementary data

Supplementary data related to this article can be found at <http://dx.doi.org/10.1016/j.carbon.2017.05.042>.

## References

- [1] G.M. Sherman, Circular dichroism of long wavelength forms of chlorophyll a, *Nature* 224 (1969) 1108–1110.
- [2] Y. He, G.K. Larsen, W. Ingram, Y. Zhao, Tunable three-dimensional helically stacked plasmonic layers on nanosphere monolayers, *Nano Lett.* 14 (4) (2014) 1976–1981.
- [3] Y. Wang, J. Deng, G. Wang, T. Fu, Y. Qu, Z. Zhang, Plasmonic chirality of L-shaped nanostructure composed of two slices with different thickness, *Opt. Express* 24 (3) (2016) 2307–2317.
- [4] J. Kaschke, J.K. Gansel, M. Wegener, On metamaterial circular polarizers based on metal N-helices, *Opt. Express* 20 (23) (2012) 26012–26020.
- [5] P.P. Wei, A.B. Tomter, A.K. Røhr, K.K. Andersson, E.I. Solomon, Circular dichroism and magnetic circular dichroism studies of the active site of p53R2 from human and mouse: iron binding and nature of the biferrous site relative to other ribonucleotide reductases, *Biochemistry* 45 (47) (2006) 14043–14051.
- [6] S.M. Kelly, T.J. Jess, N.C. Price, How to study proteins by circular dichroism, *Biochim. Biophys. Acta (BBA)-Proteins Proteom.* 1751 (2) (2005) 119–139.
- [7] F. Neubrech, A. Pucci, T.W. Cornelius, S. Karim, A. García-Etxarri, J. Aizpurua, Resonant plasmonic and vibrational coupling in a tailored nanoantenna for infrared detection, *Phys. Rev. Lett.* 101 (15) (2008) 157403.
- [8] M. Li, S.K. Cushing, N. Wu, Plasmon-enhanced optical sensors: a review, *Analyst* 140 (2) (2015) 386–406.
- [9] A.N. Sidorov, G.W. Stawiński, A.H. Jayatissa, F.P. Zamborini, G.U. Sumanasekera, A surface-enhanced Raman spectroscopy study of thin graphene sheets functionalized with gold and silver nanostructures by seed-mediated growth, *Carbon* 50 (2) (2012) 699–705.
- [10] A. Ben-Moshe, B.M. Maoz, A.O. Govorov, G. Markovich, Chirality and chiroptical effects in inorganic nanocrystal systems with plasmon and exciton resonances, *Chem. Soc. Rev.* 42 (16) (2013) 7028–7041.
- [11] Z. Zhu, W. Liu, Z. Li, B. Han, Y. Zhou, Y. Gao, Z. Tang, Manipulation of collective optical activity in one-dimensional plasmonic assembly, *ACS Nano* 6 (3) (2012) 2326–2332.
- [12] F. Lu, Y. Tian, M. Liu, D. Su, H. Zhang, A.O. Govorov, O. Gang, Discrete nanocubes as plasmonic reporters of molecular chirality, *Nano Lett.* 13 (7) (2013) 3145–3151.
- [13] E. Hendry, T. Carpy, J. Johnston, M. Popland, R.V. Mikhaylovskiy, A.J. Laphorn, S.M. Kelly, L.D. Barron, N. Gadegaard, M. Kadodwala, Ultrasensitive detection and characterization of biomolecules using superchiral fields, *Nat. Nanotechnol.* 5 (11) (2010) 783–787.
- [14] B.M. Maoz, Y. Chaikin, A.B. Tesler, O. Bar Elli, Z. Fan, A.O. Govorov, G. Markovich, Amplification of chiroptical activity of chiral biomolecules by surface plasmons, *Nano Lett.* 13 (3) (2013) 1203–1209.
- [15] A.O. Govorov, Plasmon-induced circular dichroism of a chiral molecule in the vicinity of metal nanocrystals. Application to various geometries, *J. Phys. Chem. C* 115 (16) (2011) 7914–7923.
- [16] A.O. Govorov, Z. Fan, P. Hernandez, J.M. Slocik, R.R. Naik, Theory of circular dichroism of nanomaterials comprising chiral molecules and nanocrystals: plasmon enhancement, dipole interactions, and dielectric effects, *Nano Lett.* 10 (4) (2010) 1374–1382.
- [17] M.L. Nesterov, X. Yin, M. Schäferling, H. Giessen, T. Weiss, The role of plasmon-generated near fields for enhanced circular dichroism spectroscopy, *ACS Photonics* 3 (4) (2016) 578–583.
- [18] Y. Tang, A.E. Cohen, Optical chirality and its interaction with matter, *Phys. Rev. Lett.* 104 (16) (2010) 163901.
- [19] Y. Tang, A.E. Cohen, Enhanced enantioselectivity in excitation of chiral molecules by superchiral light, *Science* 332 (6027) (2011) 333–336.
- [20] M. Schäferling, X. Yin, N. Engheta, H. Giessen, Helical plasmonic nanostructures as prototypical chiral near-field sources, *ACS Photonics* 1 (6) (2014) 530–537.
- [21] N.A. Abdulrahman, Z. Fan, T. Tonooka, S.M. Kelly, N. Gadegaard, E. Hendry, A.O. Govorov, M. Kadodwala, Induced chirality through electromagnetic coupling between chiral molecular layers and plasmonic nanostructures, *Nano Lett.* 12 (2) (2012) 977–983.
- [22] B.M. Maoz, R. van der Weegen, Z. Fan, A.O. Govorov, G. Ellestad, N. Berova, E.W. Meijer, G. Markovich, Plasmonic chiroptical response of silver nanoparticles interacting with chiral supramolecular assemblies, *J. Am. Chem. Soc.* 134 (42) (2012) 17807–17813.
- [23] E.C. Le Ru, P.G. Etchegoin, Quantifying SERS enhancements, *MRS Bull.* 38 (08) (2013) 631–640.
- [24] Z.Y. Bao, W. Zhang, Y.L. Zhang, J. He, J. Dai, C.T. Yeung, D.Y. Lei, Interband absorption enhanced optical activity in discrete Au@Ag core-shell nanocuboids: probing extended helical conformation of chemisorbed cysteine molecules, *Angew. Chem. Int. Ed.* 56 (2016) 1283.
- [25] N. Rouhi, S. Capdevila, D. Jain, K. Zand, Y.Y. Wang, E. Brown, L. Jofre, P. Burke, Terahertz graphene optics, *Nano Res.* 5 (10) (2012) 667–678.
- [26] R.W. Woody, Theory of Circular Dichroism of Proteins. In *Circular Dichroism and the Conformational Analysis of Biomolecules*, Springer US, 1996, pp. 25–68.
- [27] N. Berova, K. Nakanishi, R.W. Woody, *Circular Dichroism: Principles and Applications*, John Wiley & Sons, 2000.
- [28] Y. Hou, H.M. Leung, C.T. Chan, J. Du, H.L.W. Chan, D.Y. Lei, Ultrabroadband optical superchirality in a 3D stacked-patch plasmonic metamaterial designed by two-step glancing angle deposition, *Adv. Funct. Mater.* 26 (43) (2016) 7807.
- [29] V.V. Klimov, I.V. Zabkov, A.A. Pavlov, D.V. Guzatzov, Eigen oscillations of a chiral sphere and their influence on radiation of chiral molecules, *Opt. Express* 22 (15) (2014) 18564–18578.
- [30] J. Lekner, Optical properties of isotropic chiral media, *Pure Appl. Opt. J. Eur. Opt. Soc. Part A* 5 (4) (1996) 417.
- [31] F.H.L. Koppens, D.E. Chang, García de Abajo F.J. Graphene plasmonics: a platform for strong light–matter interactions, *Nano Lett.* 11 (8) (2011) 3370–3377.
- [32] S.A. Awan, A. Lombardo, A. Colli, G. Privitera, T.S. Kulmala, J.M. Kivioja, A.C. Ferrari, Transport conductivity of graphene at RF and microwave frequencies, *2D Mater.* 3 (1) (2016) 015010.
- [33] Y. Francescato, V. Giannini, S.A. Maier, Strongly confined gap plasmon modes in graphene sandwiches and graphene-on-silicon, *New J. Phys.* 15 (6) (2013) 063020.
- [34] S. Yuan, R. Roldán, A.P. Jauho, M.I. Katsnelson, Electronic properties of disordered graphene antidot lattices, *Phys. Rev. B* 87 (8) (2013) 085430.
- [35] N. Ligato, A. Cuppolillo, A. Sindona, P. Riccardi, M. Pisarra, L.S. Caputi, A comparative study of the plasmonic properties of graphene on lattice-matched and lattice-mismatched Ni surfaces, *Surf. Sci.* 626 (2014) 40–43.
- [36] J.A. Füst, J.G. Pedersen, C. Flindt, N.A. Mortensen, M. Brandbyge, T.G. Pedersen, A.P. Jauho, Electronic properties of graphene antidot lattices, *New J. Phys.* 11 (9) (2009) 095020.
- [37] S. Zhang, G.C. Li, Y. Chen, X. Zhu, S.D. Liu, D. Lei, H. Duan, Pronounced Fano resonance in single gold split nanodisks with 15-nm split gaps for intensive second harmonic generation, *ACS Nano* 10 (12) (2016) 11105–11114.
- [38] S.D. Liu, E.S.P. Leong, G.C. Li, Y. Hou, J. Deng, J.H. Teng, H.C. Ong, D.Y. Lei, Polarization-independent multiple Fano resonances in plasmonic nonamers for multimode-matching enhanced multiband second-harmonic generation, *ACS Nano* 10 (1) (2016) 1442–1453.
- [39] E. Carrasco, M. Tamagnone, J.R. Mosig, T. Low, J. Perruisseau-Carrier, Gate-controlled mid-infrared light bending with aperiodic graphene nanoribbons array, *Nanotechnology* 26 (13) (2015) 134002.